Volume 12
Number 29
7 August 2021
Pages 9855–10118

# Chemical Science

rsc.li/chemical-science

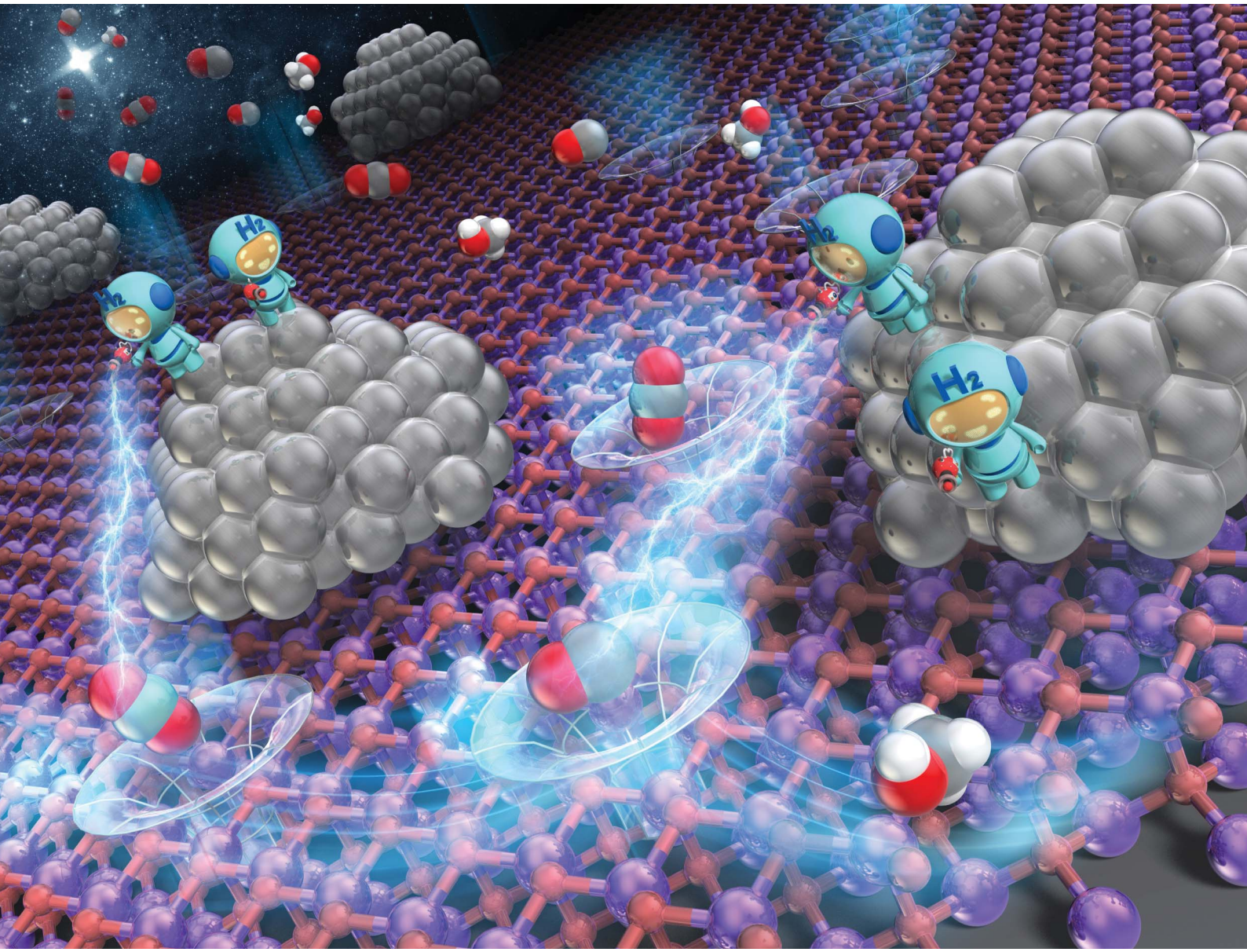


ISSN 2041-6539

ROYAL SOCIETY OF CHEMISTRY

**EDGE ARTICLE**

Yasutaka Kuwahara, Hiromi Yamashita *et al.*
A quasi-stable molybdenum sub-oxide with abundant oxygen vacancies that promotes $CO_2$ hydrogenation to methanol

Chemical Science

ROYAL SOCIETY OF CHEMISTRY

EDGE ARTICLE

View Article Online
View Journal | View Issue

Check for updates

Cite this: *Chem. Sci.*, 2021, **12**, 9902

All publication charges for this article have been paid for by the Royal Society of Chemistry

# A quasi-stable molybdenum sub-oxide with abundant oxygen vacancies that promotes $CO_2$ hydrogenation to methanol†

Yasutaka Kuwahara, *[abcd] Takashi Mihogi,[a] Koji Hamahara,[a] Kazuki Kusu,[a] Hisayoshi Kobayashi[ae] and Hiromi Yamashita *[abc]

Production of methanol from anthropogenic carbon dioxide ($CO_2$) is a promising chemical process that can alleviate both the environmental burden and the dependence on fossil fuels. In catalytic $CO_2$ hydrogenation to methanol, reduction of $CO_2$ to intermediate species is generally considered to be a crucial step. It is of great significance to design and develop advanced heterogeneous catalysts and to engineer the surface structures to promote $CO_2$-to-methanol conversion. We herein report an oxygen-defective molybdenum sub-oxide coupled with Pt nanoparticles ($Pt/H_xMoO_{3-y}$) which affords high methanol yield with a methanol formation rate of 1.53 mmol $g_{\text{-cat}}^{-1}$ $h^{-1}$ in liquid-phase $CO_2$ hydrogenation under relatively mild reaction conditions (total 4.0 MPa, 200 °C), outperforming other oxide-supported Pt catalysts in terms of both the yield and selectivity for methanol. Experiments and comprehensive analyses including *in situ* X-ray absorption fine structure (XAFS), *in situ* diffuse reflectance infrared Fourier transform (DRIFT) spectroscopy and density functional theory (DFT) calculations reveal that both abundant surface oxygen vacancies ($V_O$) and the redox ability of Mo species in quasi-stable $H_xMoO_{3-y}$ confer the catalyst with enhanced adsorption and activation capability to subsequently transform $CO_2$ to methanol. Moreover, the Pt NPs act as $H_2$ dissociation sites to regenerate oxygen vacancies and as hydrogenation sites for the CO intermediate to finally afford methanol. Based on the experimental and computational studies, an oxygen-vacancy-mediated "reverse Mars–van Krevelen (M–vK)" mechanism is proposed. This study affords a new strategy for the design and development of an efficient heterogeneous catalyst for $CO_2$ conversion.

Received 9th May 2021
Accepted 26th June 2021

DOI: 10.1039/d1sc02550c

rsc.li/chemical-science

Open Access Article. Published on 28 2021. Downloaded on 15-10-24 04.24.46.
This article is licensed under a Creative Commons Attribution-NonCommercial 3.0 Unported Licence.

## Introduction

The continuous accumulation of anthropogenic $CO_2$ in the atmosphere aggravates global warming. The control and reduction of $CO_2$ emissions have been a worldwide challenge and pressing issue. Carbon capture and storage (CCS) has been deemed as a promising technology to drastically reduce $CO_2$ emissions; however, appropriate carbon capture and utilization (CCU) technology must be developed to further reduce $CO_2$ emissions in a sustainable manner. Catalytic conversion of anthropogenic $CO_2$ into valuable chemicals is regarded as a sustainable and appealing approach to alleviate simultaneously the environmental crisis and energy demands.[1–4]

$CO_2$ is capable of being transformed to several important C1 chemicals such as CO, formic acid, methanol, and methane *via* hydrogenation.[5–9] Among those, methanol ($CH_3OH$) has attracted huge interest from industries and scientific community, because it can be used as a raw material for the production of formalin, acetic acid, olefins, and gasoline, and can be utilized as a fuel molecule for automobiles and fuel cells.[10,11] Methanol is currently produced from syngas (CO and $H_2$), generated by a steam reforming process using methane contained in liquefied natural gas (LNG) and petroleum gas (LPG), under extreme operational conditions ($T$ = 240–260 °C, $P$ = 5–10 MPa), in which Cu-based catalysts (*e.g.* $Cu/ZnO/Al_2O_3$) are used as a traditional catalyst.[5,6,12,13] Production of methanol from anthropogenic $CO_2$ existing in the atmosphere or being discharged from large stationary sources *via* hydrogenation using $CO_2$-free $H_2$ produced by renewable energy sources would be a green chemical process that could alleviate both the environmental burden and the dependence on fossil fuels.[14,15]

[a]*Division of Materials and Manufacturing Science, Graduate School of Engineering, Osaka University, 2-1 Yamada-oka, Suita, Osaka 565-0871, Japan. E-mail: kuwahara@mat.eng.osaka-u.ac.jp; yamashita@mat.eng.osaka-u.ac.jp*

[b]*Innovative Catalysis Science Division, Institute for Open and Transdisciplinary Research Initiatives (OTRI), Osaka University, 2-1 Yamada-oka, Suita, Osaka 565-0871, Japan*

[c]*Unit of Elements Strategy Initiative for Catalysts & Batteries (ESICB), Kyoto University, Katsura, Kyoto 615-8520, Japan*

[d]*JST, PRESTO, 4-1-8 Honcho, Kawaguchi, Saitama 332-0012, Japan*

[e]*Kyoto Institute of Technology, Matsugasaki, Sakyo-ku, Kyoto 606-8585, Japan*

† Electronic supplementary information (ESI) available. See DOI: 10.1039/d1sc02550c



© 2021 The Author(s). Published by the Royal Society of Chemistry

Open Access Article. Published on 28 2021. Downloaded on 15-10-24 04.24.46.
This article is licensed under a Creative Commons Attribution-NonCommercial 3.0 Unported Licence.

Direct methanol synthesis from $CO_2/H_2$ *via* gas phase hydrogenation has been implemented industrially using supported Cu catalysts; however, a low equilibrium conversion of $CO_2$ at the operational conditions is seen as a bottleneck limiting large-scale operations. Methanol synthesis from $CO_2/H_2$ ($CO_2 + 3H_2 = CH_3OH + H_2O$; $\Delta H^0_{298} = -49.5$ kJ mol$^{-1}$) is an exothermic reaction, therefore, use of lower temperature and higher pressure conditions are thermodynamically more favorable.[5,16] Recently, direct methanol synthesis in the liquid phase at lower temperatures has been studied, primarily because of easy control of the reaction temperature and easy extraction of products from the reaction system, which shifts the reaction equilibrium to the methanol production side.[17,18] Although Ru-based homogeneous catalysts are known to function as active catalysts under relatively mild conditions, addition of additive reagents to achieve high reaction rates and problems associated with product separation and catalyst recovery are critical drawbacks.[19–22] Alternatively, noble metal nanoparticle (NP) catalysts, such as Pt,[23–27] Rh,[28,29] and Re[30] *etc.* have been studied as heterogeneous catalysts for this reaction. In particular, Pt NPs are indispensable for the promotion of $CO_2$ hydrogenation due to the efficient donation of their d-orbital electrons into the $\pi^*$ antibonding system of $CO_2$. It has been reported that the activity of Pt NP catalysts is enhanced by manipulating the particle shape and the compositions (*e.g.* alloying with Co)[23,24] or by the coupling with proper support material (*e.g.* $MoS_2$),[25] leading to a high methanol yield even at a low temperature of 150 °C.

In catalytic $CO_2$ hydrogenation, activation and cleavage of the stable C=O bond of $CO_2$ to form intermediate species is generally considered to be the crucial step. Previous literatures have reported the importance of an oxygen vacancy ($V_O$) of metal oxides in the activation of $CO_2$.[31,32] For example, Bobadilla *et al.* spectroscopically understood that the oxygen vacancies of $TiO_2$ support of Au/$TiO_2$ catalyst participate in reverse water-gas shift (RWGS) reaction by activating $CO_2$.[33] Bhethanabotla and Kuhn *et al.* demonstrated that oxygen vacancy in $La_{0.75}Sr_{0.25}FeO_3$ perovskite-type oxide efficiently promotes $CO_2$ conversion in RWGS reaction.[34] Ge *et al.* demonstrated that the oxygen vacancy on the $In_2O_3$ surface assists $CO_2$ activation and hydrogenation and also stabilizes the key intermediates in $CO_2$ hydrogenation to methanol by using DFT calculation.[35] Previous studies demonstrated that oxygen vacancies formed in nonstoichiometric $WO_{3-x}$ and $MoO_{3-x}$ enable the light-assisted extraction of O atoms from $CO_2$ to form methane and CO, respectively.[36,37] Thus, the assistance of oxygen vacancies in metal oxide is deemed as an appealing approach to activate molecular $CO_2$ and weaken the C=O double bond. However, because $V_O$ sites are replenished by the dissociated O atoms during the reaction, the catalytic cycle cannot be realized. Coupling of $V_O$ sites and metal particles that simultaneously activate $H_2$ to regenerate $V_O$ sites is the key to sustaining a continuous catalytic cycle, which has been demonstrated extensively over oxide-supported metal catalysts.[33,38–40] In this regard, our group reported that oxygen-defective molybdenum sub-oxide coupled with Pt NPs (Pt/$H_xMoO_{3-y}$) can function as a reusable catalyst for hydrodeoxygenation of sulfoxide to produce sulfide under mild reaction conditions, in which abundant oxygen vacancies in $H_xMoO_{3-y}$ act as the deoxygenation site and Pt NPs act as $H_2$ dissociation sites to continuously supply active H atoms for regenerating the oxygen vacancies.[41] It is hypothesized that such a bifunctional catalytic system would be a viable catalyst for realizing simultaneous activation of $CO_2$ and $H_2$ and efficient hydrogenation of $CO_2$ to produce methanol.

In the present work, we report that an oxygen-defective molybdenum sub-oxide coupled with Pt NPs (Pt/$H_xMoO_{3-y}$) exhibits high methanol yield with a methanol formation rate of 1.53 mmol $g_{\text{-cat}}^{-1}$ $h^{-1}$ in liquid-phase $CO_2$ hydrogenation under relatively mild reaction conditions (total 4.0 MPa, 200 °C). *In situ* XAFS, *in situ* DRIFT spectroscopy and DFT calculations were employed to investigate the reaction mechanism. The experiments and comprehensive analyses revealed that abundant surface oxygen vacancies and the redox ability of Mo species in quasi-stable $H_xMoO_{3-y}$ endowed this catalyst with enhanced adsorption and activation capability to subsequently transform $CO_2$ to form the CO intermediate, and Pt NPs were found to act as $H_2$ dissociation sites to regenerate oxygen vacancies and as hydrogenation sites of CO intermediate to finally afford methanol. This study provides new insights into the design and development of high-performance heterogeneous catalysts for $CO_2$ hydrogenation reactions to produce methanol, which is a key chemical process for realizing $CO_2$ reduction and sustainable methanol production.

## Experimental

### Synthesis of oxide-supported Pt catalysts

The Pt catalyst supported on α-$MoO_3$ (Pt/$MoO_3$) was prepared by a precipitation method using urea as a precipitant.[41] α-$MoO_3$ (1.0 g) was dispersed in 100 mL of distilled water containing 4.5 mL of $K_2PtCl_4$ solution (35 mM). To this suspension, 0.2 g of urea as a precipitation reagent was added, followed by vigorous stirring for 6 h at 95 °C to precipitate $Pt^{2+}$ ions. The obtained slurry was centrifuged, washed with deionized water, and then dried at 100 °C in air overnight to give Pt/$MoO_3$ (unreduced sample). The catalyst used in the hydrogenation process was prepared by reduction of Pt/$MoO_3$ in a glass tube under a flow of $H_2$ (20 mL min$^{-1}$) for 30 min with a heating rate of 5 °C min$^{-1}$ to give Pt/$H_xMoO_{3-y}(T)$ ($T$ represents the reduction temperature (°C)). The Pt loading was determined to be 1.3 wt% by inductively coupled plasma (ICP) analysis. The Pt/$H_xMoO_{3-y}(T)$ catalysts with various Pt contents were prepared in the same manner using different amounts of $K_2PtCl_4$ solution.

Other oxide-supported Pt catalysts were prepared in the same manner described above except for using different oxides as supports. Pd, Re, Ru and Cu catalysts supported on $MoO_3$ were also prepared in the same manner described above except for using $Na_2PdCl_4$, $NH_4ReO_4$, $RuCl_3 \cdot nH_2O$, and $Cu(NO_3)_2 \cdot 3H_2O$ as the precursors, respectively, instead of $K_2PtCl_4$.

### Characterization

High-resolution transmission electron microscopy (HR-TEM) images were recorded on a JEOL ARM200F instrument operated at 200 kV accelerating voltage. The sample was dispersed in

Open Access Article. Published on 28 2021. Downloaded on 15-10-24 04.24.46.
This article is licensed under a Creative Commons Attribution-NonCommercial 3.0 Unported Licence.

ethanol by sonication, and the dispersion was dropped onto a Cu grid covered with carbon film in an Ar atmosphere to avoid sample oxidation. Power X-ray diffraction (XRD) patterns were obtained with a Rigaku Ultima IV diffractometer with Cu $K_\alpha$ radiation ($\lambda = 1.54056$ Å) operated at 40 kV and 40 mA. X-ray photoelectron spectroscopy (XPS) measurements were performed on a Shimadzu ESCA-3400 photoelectron spectrometer using Mg $K_\alpha$ radiation (1253.6 eV) X-ray source at $<10^{-5}$ Pa. Samples were introduced to the XPS analysis chamber without exposure to the air to avoid sample oxidation. All binding energies were calibrated with the adventitious carbon (C 1s) peak at 284.5 eV.

Mo K-edge and Pt L3-edge XAFS spectra were recorded at the BL01B1 beamline at the SPring-8 facility, Japan Synchrotron Radiation Research Institute (JASRI), Harima, Japan. Si(311) and Si(111) double-crystal monochromators were used for the Mo K-edge and Pt L3-edge XAFS measurements, respectively. For pseudo *in situ* XAFS measurement, the samples, pretreated in a flow of $H_2$, were sealed in a polyethylene bags without exposure to the air, and subjected to the XAFS measurement at room temperature. For *in situ* Mo K-edge XAFS measurement, a pelletized unreduced Pt/$MoO_3$ sample ($\varphi$ 7 mm) was placed in a tailor-made quartz cell (Makuhari Rikagaku Garasu Inc.) equipped with a water-cooling condenser and an electric heater, which was connected to a gas-exchange system. After purging the cell with He, the sample was first reduced at 300 °C under a flow of 20% $H_2$/He (100 mL $min^{-1}$), kept at 200 °C, and then exposed to 20% $CO_2$/He (100 mL $min^{-1}$) and 20% $H_2$/He (100 mL $min^{-1}$) in turn. During these processes, Mo K-edge XAFS spectra were recorded in transmission mode to track the changes of Mo species. The obtained XAFS spectra were normalized by fitting the background absorption coefficient. After a $k^3$-weighting, the extended XAFS (EXAFS) spectra were Fourier-transformed from the $k$ space to the $r$ space across the $k$ range $3.0 < k$ (Å$^{-1}$) $< 11.0$ to obtain the radial distribution functions (RDFs).

Temperature programmed reduction with hydrogen ($H_2$-TPR) was carried out using a BELCATII system (Microtrac-BEL Corp.) equipped with a thermal conductivity (TCD) detector. A sample (*ca.* 50 mg) mounted in a quartz vessel was pretreated in a flow of Ar (30 mL $min^{-1}$) at 150 °C for 60 min to remove the physisorbed water, and then cooled to 50 °C. TPR profiles were collected by heating the samples from 50 to 500 °C with a heating rate of 10 °C $min^{-1}$ under a flow of 5% $H_2$/Ar (50 mL $min^{-1}$). The effluent gas was passed through a trap containing a molecular sieve MS-4A to remove the produced water to determine the amount of $H_2$ consumed.

Thermogravimetric measurement (TG) was conducted in a flow of either air or $N_2$ to determine the amounts of hydrogen and oxygen vacancies introduced in molybdenum sub-oxide samples, respectively. The weight change curves were obtained on a Rigaku Thermo plus EVO II. Unreduced sample placed in an alumina pan was first reduced in a flow of $H_2$ (100 mL $min^{-1}$) at designated temperatures (100–400 °C) for 30 min, and then cooled to 50 °C. After switching the flow gas to either air or $N_2$ (100 mL $min^{-1}$), the temperature was increased from 50 to 450 °C at a heating rate of 10 °C $min^{-1}$. Based on the weight changes observed under the two different conditions, the stoichiometric compositions of the samples were determined.

### *In situ* DRIFT measurement

DRIFT spectra were measured using a Shimadzu IRSpirit spectrometer, equipped with a triglycine sulfate (TGS) detector at a resolution of 4 $cm^{-1}$. For *in situ* DRIFT measurement, unreduced sample was placed in an alumina pan, introduced into a stainless-steel heat chamber (S.T. Japan Inc.) equipped with a water-cooling system and connected to gas cylinders, and prereduced at 300 °C in a flow of $H_2$ (20 mL $min^{-1}$) for 30 min. After prereduction, the cell was kept at 250 °C and a background spectrum was obtained. Subsequently, 1.0 MPa of $CO_2$ and 1.0 MPa of $H_2$ were successively introduced into the *in situ* cell, and the DRIFT spectra were recorded every 30 min. Each DRIFT spectrum was obtained by subtracting the background spectrum from each measured spectrum.

### General procedure for $CO_2$ hydrogenation

In a typical procedure, the as-prepared catalyst (*ca.* 50 mg) was placed in a glass tube, followed by reduction at 300 °C for 30 min in a flow of $H_2$ (20 min $min^{-1}$). The glass tube containing the prereduced catalyst (*ca.* 50 mg) and 1,4-dioxane (15 mL) were placed in a stainless-steel autoclave reactor (volume = 41 mL), purged three times with pure $CO_2$, and pressurized to 1.0 MPa with $CO_2$ and then to 4.0 MPa with $H_2$ ($CO_2 : H_2 = 1 : 3$). The reactor was heated to 200 °C and magnetically stirred (600 rpm) for 20 h. After the reaction, the reaction mixture was cooled to room temperature and depressurized, and the gas products were analyzed using a gas chromatograph (GC; Shimadzu GC-8A) with a 4 m active carbon column equipped with an FID detector and a methanizer (Shimadzu MTN-1). The liquid products were analyzed using GC-FID (column: Zebron ZB-FFAP, 50 m × 0.32 mm) using 1-butanol as an external standard. The TON values were determined by dividing the quantity of $CO_2$ converted by the number of moles of the total quantity of Pt contained in the catalyst. To examine the catalyst reusability, the catalyst was retrieved from the reaction solution by centrifugation (10 000 rpm, 5 min), washed with the solvent, and then subjected to next catalytic run.

### DFT calculations

All DFT calculations were performed using the CASTEP program in Materials Studio 17.2. The Perdew–Burke–Ernzerhof exchange-correlation function within the generalized gradient approximation (GGA-PBE) with the ultrasoft core potential was employed for geometry optimization, and the double numerical plus *d*-function (DND) was chosen as the basis set. The electron configurations of the atoms were H: $1s^1$, C: $2s^2 2p^2$, O: $2s^2 2p^4$, Mo: $4s^2 4p^6 4d^5 5s^1$, Pt: $5d^9 6s^1$, the plane wave cutoff energy was set to 300 to 340 eV. Considering the layered structure of $H_{0.9}MoO_3$ in Pt/$H_xMoO_{3-y}$, a super cell slab model composed of $H_{32}Mo_{32}O_{96}$ including one Mo octahedra bilayer was constructed. The lattice parameters for the super cell are $b = 15.1776$ Å, $c = 15.4438$ Å, $\alpha = \gamma = 90°$, $\beta = 93.727°$. The *a*-axis


© 2021 The Author(s). Published by the Royal Society of Chemistry

Open Access Article. Published on 28 2021. Downloaded on 15-10-24 04.24.46.
This article is licensed under a Creative Commons Attribution-NonCommercial 3.0 Unported Licence.

was taken as the direction of surface normal, and $a$ was set to 30 Å including the vacuum region. For the slab model with a Pt NP, a $Pt_{20}$ cluster was loaded on the $H_{0.9}MoO_3$ (100) surface to model $Pt/H_xMoO_{3-y}$ catalyst.[42,43] The bottom $MoO_6$ layer was fixed at the corresponding bulk position, while the top $MoO_6$ layer, the $Pt_{20}$ cluster and the molecules in the gas phase were allowed to relax during geometry optimizations. The adsorption energy ($E_{ads}$) was defined as $E_{ads} = E_{total} - (E_{sub} + E_{molecule})$, where $E_{total}$, $E_{sub}$, and $E_{molecule}$ are the total energies of the substrate optimized together with the adsorbate, the free substrate, and the free adsorbate molecule. The activation energy for transition state (TS) was defined as the difference energy between the TS and the local minimum just before the TS.

## Results and discussion

### Liquid-phase $CO_2$ hydrogenation over oxide-supported Pt catalysts

In a preliminary study, liquid-phase $CO_2$ hydrogenation was carried out using Pt NPs catalysts immobilized on various oxide supports (Pt content: *ca.* 3 wt%) to search for a catalyst that provides a high methanol yield. The $CO_2$ hydrogenation reaction was performed using a stainless autoclave reactor (volume = 41 mL) filled with 4.0 MPa of $CO_2/H_2$ gas ($CO_2 : H_2 = 1 : 3$) at 200 °C for 20 h using catalyst (50 mg) pretreated with $H_2$ at 300 °C for 30 min (Table 1 and Fig. 1a). The main products observed in this reaction were CO, methanol, and methane. High $CO_2$ conversion rates were attained when easily reducible oxides such as $MoO_3$, $V_2O_5$, $Nb_2O_5$ and $WO_3$ were used as supports; $Pt/H_xMoO_{3-y}$ catalyst provided the highest $CO_2$ conversion (25.0%) with the highest methanol selectivity ($Sel_{MeOH}$ = 33%) among the catalysts examined, which corresponded to a 1.53 mmol yield of methanol after 20 h of reaction (methanol production rate = 1.53 mmol $g_{-cat}^{-1}$ $h^{-1}$) (entry 1), while $Pt/V_2O_5$, $Pt/Nb_2O_5$ and $Pt/WO_3$ catalysts gave CO as the main product and methanol was hardly produced ($Sel_{MeOH}$ = 5–

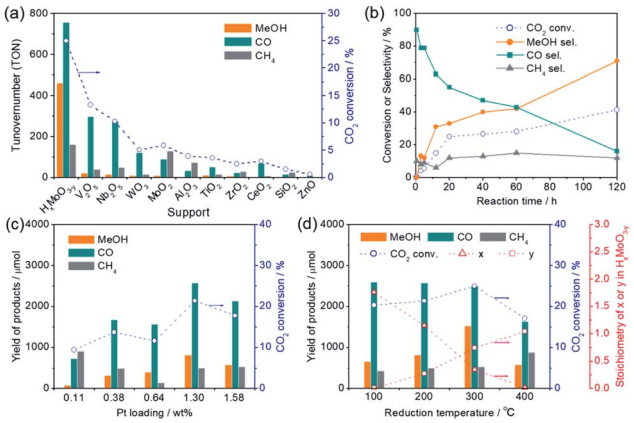


Fig. 1 (a) Comparison of catalytic performance of various oxide-supported Pt catalysts in the liquid-phase $CO_2$ hydrogenation reaction (catalysts were all reduced at 300 °C for 30 min in a flow of $H_2$). (b) Time course of the product selectivity and $CO_2$ conversion over $Pt/H_xMoO_{3-y}$(300) catalyst. (c) Effect of Pt loading on catalytic performance for $Pt/H_xMoO_{3-y}$ catalyst (catalysts were all reduced at 200 °C for 30 min in a flow of $H_2$). (d) Effect of reduction temperature on catalytic performance for $Pt/H_xMoO_{3-y}(T)$ catalyst and the stoichiometry of intercalated H atoms ($x$) and oxygen vacancies ($y$) in molybdenum sub-oxide ($H_xMoO_{3-y}$). Reaction conditions: catalyst (50 mg), 1,4-dioxane (15 mL), $P_{CO_2}$ = 1.0 MPa, $P_{H_2}$ = 3.0 MPa, 200 °C, 20 h.

Table 1 Liquid-phase $CO_2$ hydrogenation using various oxide-supported Pt catalysts[a]

| Entry | Catalyst | Metal loading[b] [wt%] | $CO_2$ conv. [%] | Selectivity [%] | | | Total TON[c] | TON for MeOH[c] |
|---|---|---|---|---|---|---|---|---|
| | | | | MeOH | CO | $CH_4$ | | |
| 1 | $Pt/H_xMoO_{3-y}$ | 1.3 | 25.0 | 33 | 55 | 12 | 1379 | 462 |
| 2 | $Pt/V_2O_5$ | 2.6 | 13.3 | 6 | 83 | 11 | 360 | 22 |
| 3 | $Pt/Nb_2O_5$ | 2.2 | 10.3 | 5 | 81 | 14 | 340 | 16 |
| 4 | $Pt/WO_3$ | 2.5 | 5.1 | 7 | 82 | 11 | 148 | 10 |
| 5 | $Pt/MoO_2$ | 1.8 | 5.9 | 4 | 39 | 57 | 231 | 10 |
| 6 | $Pt/\gamma\text{-}Al_2O_3$ | 2.6 | 3.9 | 0 | 31 | 69 | 107 | 0 |
| 7 | $Pt/TiO_2$ | 3.2 | 3.6 | 15 | 66 | 19 | 79 | 12 |
| 8 | $Pt/ZrO_2$ | 2.7 | 2.5 | 12 | 39 | 49 | 62 | 8 |
| 9 | $Pt/CeO_2$ | 2.7 | 3.0 | 4 | 86 | 10 | 81 | 3 |
| 10 | $Pt/SiO_2$ | 2.6 | 1.5 | 0 | 39 | 61 | 42 | 0 |
| 11 | Pt/ZnO | 2.8 | 0.6 | 20 | 75 | 5 | 14 | 3 |
| 12 | $Pd/MoO_3$ | 3.0[f] | 3.2 | 6 | 56 | 38 | 41 | 3 |
| 13 | $Re/MoO_3$ | 3.0[f] | 2.3 | 5 | 23 | 72 | 51 | 3 |
| 14 | $Ru/MoO_3$ | 3.0[f] | 0.9 | 37 | 50 | 13 | 12 | 4 |
| 15 | $Cu/MoO_3$[d] | 3.0[f] | 1.5 | 0 | 5 | 95 | 11 | 0 |
| 16 | Cu/ZnO[d] | 30.0[f] | 0.4 | 19 | 12 | 69 | 9 | 0.3 |
| 17 | $H_xMoO_{3-y}$[e] | — | 3.0 | 0 | 8 | 92 | — | — |
| 18 | $MoO_3$ | — | 0.3 | 0 | 21 | 79 | — | — |

[a] Reaction conditions: catalyst (50 mg), 1,4-dioxane (15 mL), $P_{CO_2}$ = 1.0 MPa, $P_{H_2}$ = 3.0 MPa, 200 °C, 20 h. Catalysts were reduced at 300 °C for 30 min in a flow of $H_2$. [b] Determined by ICP analysis. [c] TON was calculated on the basis of total active metals contained in the catalysts. [d] Prepared by the wet impregnation method. [e] Synthesized by a solvothermal method according to ref. 44. [f] Nominal content.

Open Access Article. Published on 28 2021. Downloaded on 15-10-24 04.24.46.
This article is licensed under a Creative Commons Attribution-NonCommercial 3.0 Unported Licence.

7%) (entries 2–4). For the Pt/$H_xMoO_{3-y}$ catalyst, the turnover number (TON) calculated for $CO_2$ conversion, based on the number of Pt atoms contained in the catalyst, was 1379, and the TON for methanol production was 462, demonstrating that the $CO_2$ hydrogenation reaction occurs in a catalytic manner. Interestingly, Pt supported on $MoO_2$ exhibited a lower $CO_2$ conversion (5.9%) and a lower methanol selectivity ($Sel_{MeOH}$ = 4%) compared with Pt/$H_xMoO_{3-y}$ under the same conditions (entry 5). Pt catalysts supported on amphoteric oxides, such as $Al_2O_3$, $TiO_2$, $ZrO_2$, and $CeO_2$, exhibited low $CO_2$ conversions (entries 6–9) and low methanol selectivities. As the mono-component counterparts, pristine $MoO_3$ (entry 18), defective $H_xMoO_{3-y}$ (prepared by a solvothermal method)[44] (entry 17) and Pt/$SiO_2$ catalyst (entry 10) were also examined; however, the $CO_2$ conversions (0.3%, 3.0% and 1.5%, respectively) over these catalysts in 20 h were far below that of the Pt/$H_xMoO_{3-y}$ catalyst and the formation of methanol was not observed. It was thus clarified that the nature of the oxide support has a dramatic effect on the catalytic performance of the Pt catalyst in liquid-phase $CO_2$ hydrogenation. In addition, Pd, Re, Ru, and Cu catalysts supported on $MoO_3$ (entries 12–15), which were prepared by a similar method (see Experimental section), and Cu/ZnO catalyst (entry 16; nominal Cu content = 30.0 wt%) traditionally used for gas-phase $CO_2$ hydrogenation reaction showed low catalytic activities and low methanol yields under the conditions adopted in this study. The significantly low catalytic activity observed for the benchmark Cu/ZnO catalyst may be attributed to the use of organic solvent which is unmatched for Cu-based catalyst and a relatively lower operation temperature than that usually employed for Cu-based catalysts. These results indicate that Pt is an indispensable component in the catalytic reaction, and the synergetic effect between Pt and Mo sub-oxide plays a critical role in achieving a high catalytic performance.

### Liquid-phase $CO_2$ hydrogenation over molybdenum oxide-supported Pt catalyst

Fig. 1b shows the time variation of product yields during the reaction on the Pt/$H_xMoO_{3-y}$(300) at 200 °C. CO was rapidly produced as the main product in the initial stage of the reaction and yields of methanol and methane steadily increased over time along with a gradual decrease in the yield of CO. The conversion of $CO_2$ and the selectivity for methanol obtained at 200 °C after 120 h of reaction reached 41.4% and 71%, respectively, which corresponded to a 5.38 mmol yield of methanol (methanol production rate = 0.896 mmol $g_{\text{-cat}}^{-1}$ $h^{-1}$). The decreased conversion rate of $CO_2$ in the latter stage of reaction may reflect the gradual reduction of $CO_2/H_2$ gas pressures inside the reactor. In methanol synthesis from $CO_2$ and $H_2$, (i) the CO formation route and (ii) the $HCOO^-$ (formate) formation route are known to be major reaction pathways.[6,45,46] Considering the product distribution and the fact that formate was not detected by liquid chromatography in the reaction solution, methanol is likely to be produced *via* the formation of CO as an intermediate (*i.e.* RWGS reaction), while a small fraction of CO is transformed irreversibly to methane.

Fig. 1c shows the effect of the loading amount of Pt on the catalytic activity. The highest yield and selectivity for methanol formation was achieved when the Pt loading was 1.3 wt%. Although the conversion of $CO_2$ and the yield of methanol tended to increase with increasing Pt loading, they decreased when the Pt loading exceeded 1.5 wt%. Pt L3-edge XAFS analysis (Fig. S1 in ESI†) and Pt 4f XPS spectra (Fig. S2 in ESI†) verified that the Pt species on these catalysts exist as metallic Pt(0) NPs in all cases and the size of the Pt NPs increases with increasing Pt content. The catalytic activity was not directly proportional to the mean surface area of surface-exposed Pt atoms determined by CO pulse measurement (Fig. S3 in ESI†), suggesting that the $CO_2$ hydrogenation is catalyzed not solely on the Pt NPs surface, but at the interface between the Pt NPs and the $H_xMoO_{3-y}$ support, and that larger Pt NPs are unfavorable due to a decrease in the number of Pt–$H_xMoO_{3-y}$ interfacial sites.

Over the Pt/$H_xMoO_{3-y}$(300) catalyst, almost no product was detected in the absence of $CO_2$ (trace of $CH_4$ may be from carbonaceous species contained in the catalyst) (Table 2, entry 2). In fact, in an isotopic experiment using $^{13}CO_2$ as a reaction gas instead of $^{12}CO_2$, a signal at $m/z$ = 33 assigned to $^{13}CH_3OH$ was detected (Fig. S4 in ESI†), confirming that $CO_2$ is the sole carbon source for CO, methanol and methane. More noteworthy is the fact that a substantial amount of CO was produced even in the absence of $H_2$ (entry 3). Considering that such a huge CO

Table 2 Methanol production *via* $CO_2$ hydrogenation using Pt/$H_xMoO_{3-y}$(300) catalyst under different conditions[a]

| | | | Yield [μmol] | | | |
|---|---|---|---|---|---|---|
| Entry | Conditions | $CO_2$ conv. [%] | MeOH | CO | $CH_4$ | Total TON[b] |
| 1 | $P_{CO_2}$ = 1.0 MPa<br>$P_{H_2}$ = 3.0 MPa | 25.0 | 1526 | 2501 | 532 | 1379 |
| 2 | No $CO_2$<br>$P_{H_2}$ = 3.0 MPa | 0 | 0 | <1 | 66 | — |
| 3 | $P_{H_2}$ = 1.0 MPa<br>No $H_2$ | 10.9 | 0 | 1541 | 443 | 600 |
| 4 | $P_{CO_2}$ = 0.1 MPa<br>$P_{H_2}$ = 3.0 MPa | (CO conv.) 57.8 | 371 | — | 684 | 310 |

[a] Reaction conditions: catalyst (Pt/$H_xMoO_{3-y}$(300), 50 mg), 1,4-dioxane (15 mL), 200 °C, 20 h. [b] TON was calculated on the basis of total Pt atoms contained in the catalyst.


© 2021 The Author(s). Published by the Royal Society of Chemistry

Open Access Article. Published on 28 2021. Downloaded on 15-10-24 04.24.46.
This article is licensed under a Creative Commons Attribution-NonCommercial 3.0 Unported Licence.

evolution was not observed on most of the other supported Pt catalysts (Fig. S5 in ESI†), the oxygen vacancies created on $H_x$-$MoO_{3-y}$ possibly functioned as deoxygenation sites to reduce $CO_2$ to CO. Furthermore, introduction of CO (0.1 MPa) instead of $CO_2$ resulted in the formation of substantial amounts of methanol and methane at 200 °C (entry 4), again confirming that methanol as well as methane are produced *via* hydrogenation of CO as an intermediate over the Pt/$H_x$$MoO_{3-y}$(300) catalyst.

### Structural analysis of Pt-loaded molybdenum oxide

The HR-TEM image of the Pt/$H_x$$MoO_{3-y}$(300) catalyst revealed that the Pt NPs with an average particle size of 2.4 nm are uniformly immobilized on the Mo oxide particles (Fig. 2a).

In the enlarged HR-TEM image, the interplanar distance of the Pt NPs was *ca.* 1.95 Å, matching well the (200) plane of fcc Pt (Fig. 2b). The lattice fringes seen in the Mo oxide particle were not clear, being considerably disconnected or distorted in most cases (Fig. 2c). Only a few diffraction spots were observable in the selected electron diffraction (SAED) pattern (inset in Fig. 2c), indicating a short-range order atomic arrangement, which may be because of the introduction of many defect sites. Meanwhile, some clear lattice fringes were partly observed in some Mo oxide particles (Fig. 2d), which are consistent with the *d*-spacing of the (001) and (010) planes of the monoclinic $H_{0.9}MoO_3$ phase.[47–49] The corresponding SAED pattern exhibited clear spots assignable to the (001) and (010) planes (inset in Fig. 2d). Two interplanar spacings were found to be 0.41 and 0.37 nm with a separation angle of 91–92°, which matched well with the monoclinic structure of the $H_{0.9}MoO_3$ phase with the $P2_1/c$ space group as shown in Fig. 2e, confirming the existence of crystalline $H_{0.9}MoO_3$ phases in the short-range order.

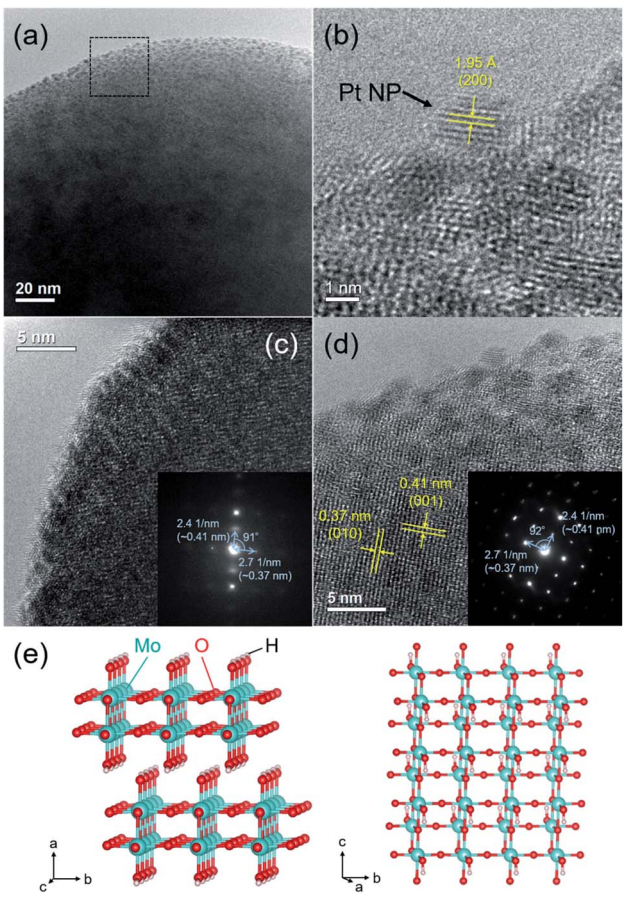


Fig. 2 (a) HR-TEM image, (b–d) magnified HR-TEM images (inset shows the corresponding SAED patterns of the Pt/$H_x$$MoO_{3-y}$(300)) catalyst, and (e) illustrations of the monoclinic $H_{0.9}MoO_3$ crystal structure.

Interestingly, the catalytic activity of the Pt/$H_x$$MoO_{3-y}$ catalyst varied with the temperature of $H_2$ reduction (Fig. 1d); both the $CO_2$ conversion and the yield of methanol tended to increase with increasing reduction temperature. In particular, the highest $CO_2$ conversion (25%) and methanol selectivity (33%) were attained when the catalyst was reduced at 300 °C. However, a marked drop of catalytic performance (conv. = 17.1%, $Sel_{MeOH}$ = 19%) was observed for reduction at 400 °C. $H_2$-TPR is commonly used to help understand the reduction behavior of metal oxides. Fig. 3a compares the $H_2$-TPR profiles of the as-synthesized oxide-supported Pt catalysts. The as-prepared Pt/$MoO_3$ sample gave an intense reduction peak at 136 °C, while such a large $H_2$ consumption was not observed for the other oxide-supported Pt catalysts. The amount of $H_2$ consumed below 200 °C was calculated to be 4.95 mmol-$H_2$ per g-catalyst. The molar ratio of H atoms consumed per mole of Pt atoms contained in the catalyst (H/Pt) was 149 and that used per mole number of Mo atoms (H/Mo) was 1.44, whereas the as-prepared Pt/$SiO_2$ showed a quite low consumption of $H_2$ (H/Pt molar ratio of 2.2). This result indicates that the large $H_2$ consumption on Pt/$MoO_3$ at around 136 °C is not only due to the reduction of the Pt precursor but is attributed to the reduction of the $MoO_3$ support. An additional $H_2$ consumption at around 280 °C may be associated with the formation of oxygen vacancies, as will be discussed later. Importantly, pristine $MoO_3$ exhibited no $H_2$ consumption below 500 °C, indicating that Pt assists in the reduction of the $MoO_3$ support by facilitating the dissociation of molecular $H_2$ (namely, the H-spillover process). Such a high reactivity of intracrystalline oxygen atoms in $MoO_3$ may well be responsible for the high $CO_2$ hydrogenation performance.

To track the crystallographic changes occurring with $H_2$ reduction at the different temperatures, XRD measurements were performed (Fig. 3b). The diffraction patterns of Pt/$H_x$-$MoO_{3-y}$(100) were assigned to orthorhombic α-$MoO_3$ (PDF #5-0508) and monoclinic $H_{0.9}MoO_3$ (PDF #53-1024), while the peaks of unreduced Pt/$MoO_3$ were all indexed to orthorhombic α-$MoO_3$. Pt/$H_x$$MoO_{3-y}$(200) showed dominant peaks assigned to $H_{0.9}MoO_3$ with decreased diffraction intensities, and Pt/$H_x$-$MoO_{3-y}$(300) exhibited almost no distinct diffractions, indicating a collapse of the $H_{0.9}MoO_3$ phase and a disordered atomic arrangement (the $H_{0.9}MoO_3$ phase may partly exist, as observed by HR-TEM). The orthorhombic α-$MoO_3$ used as a support in this study is composed of edge-sharing $MoO_6$ octahedra bilayers stacked along with [010] due to van der Waals interaction.[50,51] As demonstrated in many previous studies, H-spillover occurs on noble metal catalysts supported

Open Access Article. Published on 28 2021. Downloaded on 15-10-24 04.24.46.
This article is licensed under a Creative Commons Attribution-NonCommercial 3.0 Unported Licence.

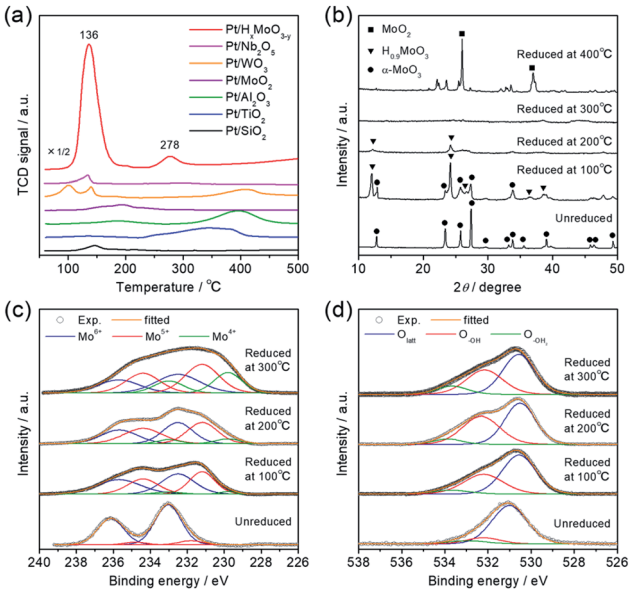


Fig. 3 (a) $H_2$-TPR profiles of Pt catalysts supported on various metal oxides. (b) XRD patterns, (c) Mo 3d XPS spectra, and (d) O 1s XPS spectra of unreduced Pt/$MoO_3$ and Pt/$H_xMoO_{3-y}$ catalysts reduced with $H_2$ at different temperatures.

on reducible metal oxides in the presence of $H_2$, in which molecular $H_2$ is dissociated over the noble metal NPs surface ($H_2 \rightarrow 2H^+ + 2e^-$) and thus protons ($H^+$) and free electrons are concurrently injected into the metal oxide matrices.[52,53] In the case of the combination of the Pt NPs and α-$MoO_3$, $H_2$ dissociation occurs on the Pt NPs at around 140 °C (as shown in the $H_2$-TPR, see Fig. 3a), and the dissociated $H^+$ atoms are coordinated to the interlayer terminal oxygen atoms to form hydroxyl groups, which yields a class of $H_xMoO_3$ materials ($0 < x < 2$), namely, hydrogen molybdenum bronze,[47–49] as depicted in the schematic of Scheme 1. During this H-spillover process, the free electrons are trapped by $Mo^{6+}$ ions ($Mo^{6+} + e^-/2e^- \rightarrow Mo^{5+}/Mo^{4+}$), and thus a great number of low-valence Mo species are generated. The relevant intercalation chemistry on α-$MoO_3$ is already well established by earlier studies.[41–43,54–57] A further temperature increase to 200–300 °C causes dehydration of $H_xMoO_3$ (as shown in the $H_2$-TPR, see Fig. 3a), in which lattice oxygen atoms (mainly bi-bridging oxygen atoms) are easily expelled by the $H^+$ ions ($2H^+ + 2e^- + O_O \rightarrow V_O + H_2O$),[58,59] thus resulting in a further greater reduction of $H_xMoO_3$ to the quasi-stable $H_xMoO_{3-y}$ sub-oxide which has abundant oxygen vacancies. Introduction of massive amounts of oxygen vacancies causes order-disorder transitions in the metal oxide (as illustrated in Scheme 1), which accounts for the significantly decreased diffraction intensities for Pt/$H_xMoO_{3-y}$(200) and Pt/$H_xMoO_{3-y}$(300). As previously reported, the intercalation of H atoms and the introduction of oxygen vacancies into the $MoO_3$ matrix increases the electron density of the entire oxide particle, fills the 4d Mo level, and brings about new energy levels near the conduction band (CB), which consequently leads to the emergence of new absorption bands due to surface plasmon resonance (SPR).[41,60–62] This was corroborated by UV-vis-NIR measurement (Fig. S6 in ESI†), in which a strong absorption across the visible to NIR region with an intense SPR peak was observed for the reduced samples, while a limited absorption in the UV region was observed for the unreduced Pt/$MoO_3$ sample. Further increase in the reduction temperature to 400 °C led to the transition to the $MoO_2$ phase, which has a distorted monoclinic rutile structure.

The intercalation of H atoms and the formation of oxygen vacancies within the Mo oxide matrices upon $H_2$ reduction was corroborated by XPS measurement. From the Mo 3d XPS spectrum (Fig. 3c), it was confirmed that low-valence Mo species ($Mo^{5+}/Mo^{4+}$) were formed after $H_2$ reduction, while $Mo^{6+}$ species mainly existed before reduction. The concentrations of these low-valence Mo species increased with rise in the reduction temperature. The proportion of these low-valence Mo species was determined as: $Mo^{5+}$ 42.7%, $Mo^{4+}$ 3.8% (100 °C reduction) → $Mo^{5+}$ 47.6%, $Mo^{4+}$ 8.2% (200 °C reduction) → $Mo^{5+}$ 42.0%, $Mo^{4+}$ 23.7% (reduction at 300 °C), suggesting that generation of $Mo^{4+}$ mainly results from the formation of an oxygen vacancy.[63] A similar reduction behavior for Mo species and the introduction of oxygen vacancies were corroborated by inspection of the Mo K-edge X-ray absorption near edge structure (XANES) spectra and the Fourier transforms of extended XAFS (EXAFS)

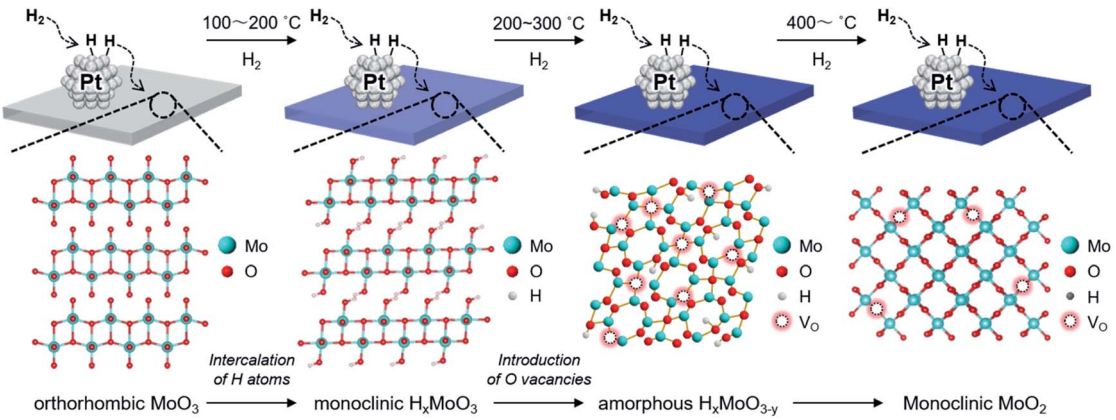


Scheme 1 Schematic illustration of the crystallographic changes of Pt/$H_xMoO_{3-y}$ upon $H_2$ reduction.


© 2021 The Author(s). Published by the Royal Society of Chemistry

Open Access Article. Published on 28 2021. Downloaded on 15-10-24 04.24.46.
This article is licensed under a Creative Commons Attribution-NonCommercial 3.0 Unported Licence.

spectra, respectively (see Fig. S7 in ESI; † see also Fig. 5). In the O 1s XPS spectra (Fig. 3d), unreduced Pt/$MoO_3$ exhibited two main peaks which are ascribed to lattice oxygen ($O_{latt}$; 530.5 eV) and surface hydroxyl groups ($O_{-OH}$; 532.3 eV). Note that the samples were introduced to the XPS analysis chamber without exposure to the air, thereby excluding the possibility of adsorbed oxygen species. For the series of Pt/$H_xMoO_{3-y}$ samples, the peak for the $O_{-OH}$ species increased in intensity, and additional tailings, assigned to the formation of $OH_2$ groups weakly coordinated to Mo atoms ($O_{-OH_2}$), were observed at the higher binding energy region at about 533.6 eV. The proportion of these hydroxyl species (($O_{-OH}$ + $O_{-OH_2}$)/$O_{total}$) was found to increase significantly upon $H_2$ reduction (unreduced Pt/$MoO_3$ (20.3%) → Pt/$H_xMoO_{3-y}$ (41–49%)), evidencing the $H^+$-intercalation upon $H_2$ reduction process.[64]

The above results verify the co-existence of the intercalated H atoms and oxygen vacancies in Pt/$H_xMoO_{3-y}$, which accompanies the formation of low-valence Mo species. To quantify the amounts of doped H atoms and oxygen vacancies, TG analysis was performed.[65,66] Upon heat treatment of oxygen-defective $H_xMoO_{3-y}$ in an inert gas flow, a dehydration reaction may occur through eqn (1):

$$H_xMoO_{3-y} \rightarrow MoO_{3-y-x/2} + 1/2x\ H_2O \quad (1)$$

However, upon heat treatment in an air gas flow, both the dehydration reaction and a filling of the oxygen vacancies to form molybdenum trioxide ($MoO_3$) possibly occur through eqn (2):

$$H_xMoO_{3-y} + O_2\ (air) \rightarrow MoO_3 + 1/2x\ H_2O \quad (2)$$

Therefore, the stoichiometry of the doped H atoms ($x$) and the oxygen vacancies ($y$) in $H_xMoO_{3-y}$ can be calculated from the changes in thermal weight observed under the two different conditions (Fig. S8 in ESI†). Assuming the composition of the oxygen-defective molybdenum oxide of $H_xMoO_{3-y}$, the composition was determined as $H_{1.76}MoO_{2.99}$ (100 °C reduction) → $H_{1.15}MoO_{2.72}$ (200 °C reduction) → $H_{0.35}MoO_{2.26}$ (300 °C reduction) from the results of TG analysis, showing that the intercalated H atoms are continuously removed *via* thermal dehydration, while an increased number of oxygen vacancies is introduced after $H_2$ reduction at elevated temperatures. As shown in Fig. 1d, the $CO_2$ conversion and the yield of methanol increased along with an increase in the stoichiometry of the oxygen vacancy ($y$) in the Pt/$H_xMoO_{3-y}$($T$) catalysts in the reduction temperature range of 100 to 300 °C. It should be mentioned that the stoichiometry of $x$ and $y$ in the Pt/$H_xMoO_{3-y}$(400) catalyst was almost equal to 0.0 and 1.0, respectively, indicating the formation of $MoO_2$, which is consistent with XRD data (Fig. 3b). The decreased activity for Pt/$H_xMoO_{3-y}$(400) is probably attributed to the transition to monoclinic $MoO_2$ with less oxygen vacancies. These results indicate the possibility that the oxygen vacancies formed in the quasi-stable $H_xMoO_{3-y}$ sub-oxide during $H_2$ reduction play a pivotal role in the $CO_2$ hydrogenation and in the production of methanol.

## Understanding the role of the oxygen vacancy

$CO_2$ adsorption is generally regarded as being a prerequisite in the $CO_2$ reduction process. Based on the above experiments, it may be hypothesized that the presence of abundant surface oxygen vacancies endows the Pt/$H_xMoO_{3-y}$ with enhanced $CO_2$ adsorption, leading to an efficient activation of $CO_2$ on the surface. This was verified by the $CO_2$ adsorption measurement (Fig. S9 in ESI†). The Pt/$H_xMoO_{3-y}$(300), which possessed the highest oxygen vacancy concentration, showed a much higher $CO_2$ adsorption capacity than the unreduced Pt/$MoO_3$.

To understand the role of the oxygen vacancy at an atomic level, the $CO_2$ adsorption energies over the surface of oxygen-defective and perfect molybdenum oxide were calculated using density function theory (DFT) calculations. Considering the layered structure of $H_{0.9}MoO_3$ in the Pt/$H_xMoO_{3-y}$ catalyst, the (100) surface of $H_{0.9}MoO_3$ was chosen to construct the slab model. For oxygen-defective slab model, oxygen vacancy was created at the bi-bridging oxygen atom position.[58,59] The adsorption energy of $CO_2$ on the oxygen-defective $H_{30}Mo_{32}O_{95}$ surface was calculated to be −8.3 kcal $mol^{-1}$, which was significantly higher than that on the perfect $H_{30}Mo_{32}O_{96}$ surface (−0.23 kcal $mol^{-1}$), indicating that an oxygen defect site is favorable for adsorption of $CO_2$.[67,68] When $CO_2$ is adsorbed at the oxygen vacancy site, the $CO_2$ molecule becomes bent, and the O–C–O angle changes from 179.2° to 125.1°, and the C–O bond length is extended from 1.178 Å to 1.224/1.370 Å (Fig. 4a), while those adsorbed on the perfect surface were unchanged (Fig. 4b).[68] These findings indicate that the C–O bonds are weakened on the oxygen-defective $H_{30}Mo_{32}O_{95}$ surface. Furthermore, Mulliken population analysis demonstrated that the total charge ($\Delta q$) of $CO_2$ is increased from +0.0$e$ (on perfect $H_{30}Mo_{32}O_{96}$) to −0.47$e$ (on oxygen-defective $H_{30}Mo_{32}O_{95}$).[68] The $CO_2$ molecule adsorbed on an oxygen vacancy gains more electrons from the low-valence Mo ions (*i.e.* $Mo^{5+}$/$Mo^{4+}$ species) with partially higher electron densities, which leads to polarization of $CO_2$, which, therefore, promotes the activation and dissociation of the $CO_2$ molecule.

To understand the catalytic role of the oxygen vacancy in $CO_2$ hydrogenation, *in situ* XAFS measurement was performed.

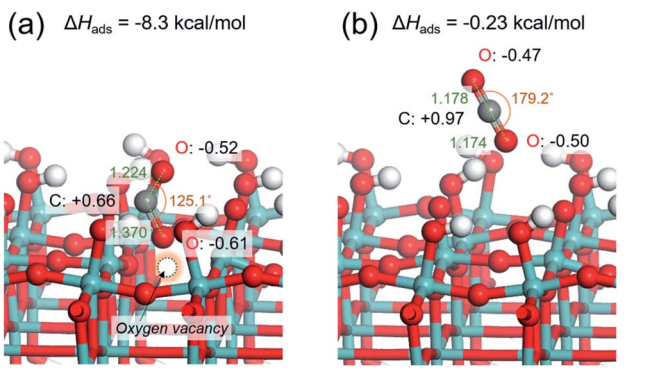


Fig. 4 Optimized structure models for $CO_2$ adsorbed on (a) oxygen-defective $H_xMoO_{3-y}$ ($H_{30}Mo_{32}O_{95}$) surface and (b) perfect $H_xMoO_3$ ($H_{30}Mo_{32}O_{96}$) surface.

Open Access Article. Published on 28 2021. Downloaded on 15-10-24 04.24.46.
This article is licensed under a Creative Commons Attribution-NonCommercial 3.0 Unported Licence.

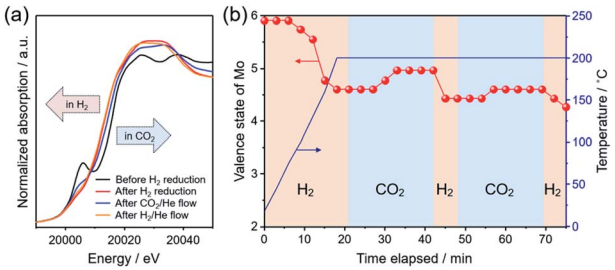


Fig. 5 (a) *In situ* Mo K-edge XANES spectra of $Pt/MoO_3$ measured at 200 °C; before $H_2$ reduction (black line), after $H_2$ reduction under a flow of 20% $H_2$/He (red line), after subsequent flow of 20% $CO_2$/He (blue line) and subsequent flow of 20% $H_2$/He (orange line). (b) Change of valence state of the Mo species during the *in situ* XAFS measurement. The valence state was determined by a linear interpolation method.

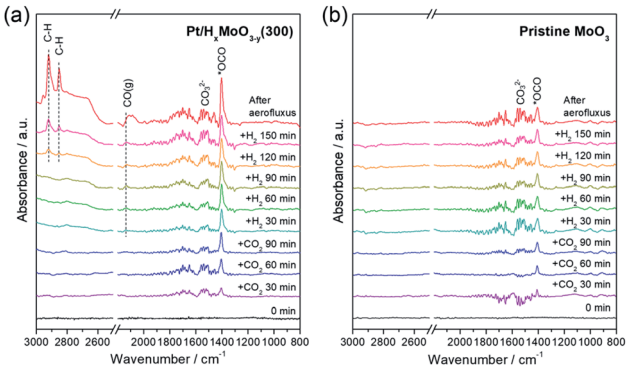


Fig. 6 *In situ* differential DRIFT spectra of adsorbed species on (a) Pt/$H_xMoO_{3-y}$(300) catalyst and (b) pristine $MoO_3$.

Fig. 5a shows the XANES spectra in the Mo K-edge region for the as-prepared $Pt/MoO_3$ sample before and after $H_2$ reduction at 200 °C, and for those measured after subsequent exposure to $H_2$ and $CO_2$ at 200 °C. The as-prepared $Pt/MoO_3$ sample exhibited an absorption spectrum with a characteristic pre-edge absorption at 20 006 eV, which was almost the same as that of orthorhombic α-$MoO_3$. After $H_2$ reduction at 200 °C, the pre-edge absorption was significantly diminished and the absorption edge position clearly shifted towards the lower energy region, which led to an absorption spectrum close to that of monoclinic $MoO_2$. This is because of the phase transition from the orthorhombic α-$MoO_3$ with a distorted octahedral geometry to the $H_xMoO_{3-y}$ sub-oxide with a symmetric octahedral geometry and low-valence Mo atoms.[69,70] Such a spectral change upon $H_2$ reduction is consistent with the results of XRD and Mo 3d XPS. After the introduction of the 20% $CO_2$/He flow gas at 200 °C, the absorption edge shifted slightly towards the higher energy region, showing substantial oxidation of Mo species with $CO_2$. The subsequent switching to 20% $H_2$/He flow caused an absorption edge shift back towards the lower energy region, indicating a re-reduction of Mo species with $H_2$. The average valence state of Mo ions in the catalyst during the *in situ* XAFS measurement was determined from the absorption edge position ($E_0$) using a linear interpolation method and was plotted as a function of time. As shown in Fig. 5b, the average valence state of Mo increased/decreased reversibly for the $CO_2/H_2$ flow at 200 °C, clearly demonstrating that a redox event involving the Mo species took place during reduction of $CO_2$. The molybdenum oxide is initially reduced by H atoms dissociated on Pt NPs through a H-spillover process to produce oxygen vacancies. The $CO_2$ molecule is adsorbed and activated at the oxygen vacancy interbedded between the under-coordinated Mo ($Mo^{5+}$/$Mo^{4+}$) sites, which leads to the formation of CO and a concurrent replenishment of the oxygen vacancy ($CO_2 + V_O \rightarrow CO + O_O$) accompanied by the oxidation of Mo atoms. This was also corroborated by Mo 3d XPS spectra, in which the proportion of $Mo^{4+}$ species considerably decreased and the average oxidation number of Mo increased upon a treatment with 1.0 MPa $CO_2$ at 200 °C (Fig. S10 in ESI†). In the presence of $H_2$, the oxygen vacancy can be regenerated by the reaction with H atoms, thus the catalytic cycle can be achieved. This process can be understood as an oxygen-vacancy-mediated "reverse Mars–van Krevelen (M–vK)[71]" mechanism.[31,33,41,72] Thus, DFT calculations and *in situ* XAFS measurement revealed that the oxygen vacancy sites in oxygen-defective $H_xMoO_{3-y}$ not only stabilize $CO_2$ by donating electrons, but also promote dissociation of $CO_2$ through electron transfer from the abundant localized electrons on the ionic Mo ($Mo^{5+}$/$Mo^{4+}$) species to $CO_2$, which should be effective for promoting the cleavage of $CO_2$ and the subsequent hydrogenation reactions.

## The $CO_2$ hydrogenation mechanism

To monitor the $CO_2$ hydrogenation process, *in situ* DRIFT experiments were performed (Fig. 6). Prior to DRIFT spectra measurement, the as-synthesized $Pt/MoO_3$ sample was pretreated under $H_2$ flow for 30 min at 300 °C to yield $Pt/H_xMoO_{3-y}$(300), followed by cooling to 250 °C, and then 1.0 MPa of $CO_2$ and 2.0 MPa of $H_2$ were successively introduced.

After the introduction of $CO_2$, two distinct peaks were observed at 1404 and at around 1530 $cm^{-1}$, the former being commonly assigned to symmetric stretching vibration mode of monodentate carbonate species ($\nu_s(OCO^-)$) (major species) and the latter being characteristic of the C=O stretching vibration of bidentate carbonates (minor species).[23,73–75] After the introduction of $H_2$, a broad band assignable to gaseous CO was observed at around 2130 $cm^{-1}$,[74–76] indicating that the $CO_2$ adsorbed on the catalyst underwent deoxygenation to produce CO, although such a peak was not observed before $H_2$ introduction because of only a small yield of CO. Along with the increase in time, several additional features associated with the hydrogenated products were observed with increased IR intensity; the peaks observed at 2851 and 2922 $cm^{-1}$ are assignable to stretching vibrations of C–H bond.[76,77] The tailing band observed at around 1300–1400 $cm^{-1}$ is assignable to hydroxyl O–H deformation vibration and $CH_3$ deformation vibration. The emergence of these bands indicate the formation of methanol over the $Pt/H_xMoO_{3-y}$(300) catalyst *via* hydrogenation of activated $CO_2$ intermediates or gaseous CO. IR bands associated with formate intermediates were not detected by *in situ* DRIFT


© 2021 The Author(s). Published by the Royal Society of Chemistry

Open Access Article. Published on 28 2021. Downloaded on 15-10-24 04.24.46.
This article is licensed under a Creative Commons Attribution-NonCommercial 3.0 Unported Licence.

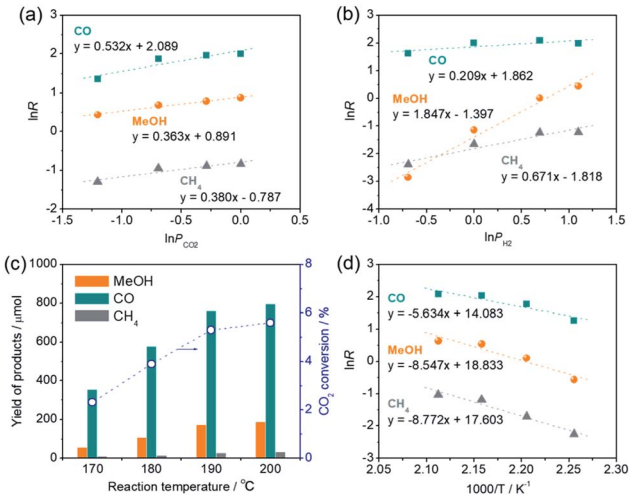


Fig. 7 (a) Double logarithm plots of reaction rate ($R$) and the partial pressure of $CO_2$ ($P_{CO_2}$), (b) double logarithm plots of reaction rate ($R$) and the partial pressure of $H_2$ ($P_{H_2}$), (c) effect of reaction temperature on catalytic performance, and (d) Arrhenius plots for the Pt/$H_x$-$MoO_{3-y}$(300) catalyst. Reaction conditions: catalyst (50 mg), 1,4-dioxane (15 mL), reaction time = 2 h.

analysis, again elucidating that hydrogenation of $CO_2$ on Pt/$H_xMoO_{3-y}$ catalyst occurs *via* the "RWGS-CO pathway". It is also noteworthy that CO/methanol were produced even in the absence of solvent, demonstrating the availability of Pt/$H_x$-$MoO_{3-y}$ catalyst in gas-phase $CO_2$ hydrogenation reaction to produce CO/methanol. In contrast, the intensity of the IR band for $CO_2$ adsorbed on pristine $MoO_3$ was apparently less than that adsorbed on Pt/$H_xMoO_{3-y}$(300), indicating a much larger amount of adsorption sites for $CO_2$ exists on Pt/$H_xMoO_{3-y}$(300). Furthermore, the IR bands associated with the hydrogenated carbon products were scarcely observed on pristine $MoO_3$, demonstrating the role of Pt NPs as a hydrogenation center.

The reaction rate ($R$) of $CO_2$ hydrogenation can be expressed by $R = k \times P_{CO_2}{}^{\alpha} \times P_{H_2}{}^{\beta}$, where $k$ is the rate constant, $P_{CO_2}$ and $P_{H_2}$ represent the partial pressure of $CO_2$ and $H_2$, and $\alpha$ and $\beta$ represent the reaction order of $CO_2$ and $H_2$, respectively. Kinetic analyses demonstrated that the reaction order of $CO_2$ ($\alpha$) for CO production (0.532) was apparently larger than those for methanol production (0.363) and $CH_4$ production (0.380), indicating that the CO formation step is primarily governed by the $CO_2$ pressure and $H_2$ is rarely involved in this step. However, the reaction orders of $H_2$ ($\beta$) for methanol production (1.847) and $CH_4$ production (0.671) were much larger than that for CO production (0.209), indicating that methanol and $CH_4$ are produced from a CO intermediate *via* hydrogenation and the methanol production rate is strongly dependent on the $H_2$ pressure. These results are consistent with the conclusions drawn by catalytic experiments and the *in situ* DRIFT spectra measurement whereby CO is produced *via* deoxygenation of $CO_2$ at the oxygen vacancy sites and methanol and $CH_4$ are produced *via* hydrogenation of the CO on the Pt NPs. Furthermore, the reaction order of $H_2$ ($\beta$) for methanol production (1.847) was close to 2, which is consistent with the stoichiometric ratio of the CO hydrogenation reaction to produce methanol ($CO + 2H_2 \rightarrow CH_3OH$). Reaction rates decreased as the reaction temperature was lowered (Fig. 7c), although methanol synthesis from $CO_2/H_2$ favors lower reaction temperature due to an exothermic reaction. This is probably because of the RWGS reaction, an endothermic process ($CO_2 + H_2 = CO + H_2O$; $\Delta H^0_{298} = 41.2$ kJ mol$^{-1}$), dominantly takes place in the early stage of reaction. From the Arrhenius plots, the activation energies for the production of CO, methanol, and $CH_4$ were determined as 46.8, 71.1, and 72.9 kJ mol$^{-1}$, respectively (Fig. 7d), verifying that the former deoxygenation reaction of $CO_2$ to produce CO is energetically more favorable than the latter hydrogenation reactions of the CO intermediate.

To draw a possible reaction pathway for $CO_2$ hydrogenation whereby methanol is produced over the Pt/$H_xMoO_{3-y}$ catalyst, DFT calculations using the periodic slab model were performed. Based on the HR-TEM observation results and previous literature,[42,43] a slab model composed of a $Pt_{20}$ cluster immobilized on the (100) exposed surface of $H_{30}Mo_{32}O_{96}$ of which the

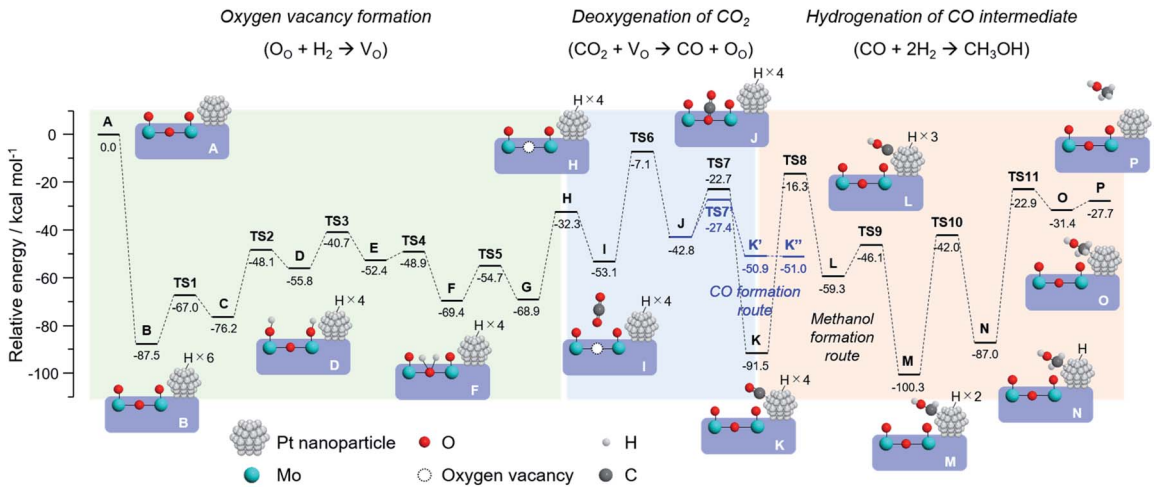


Fig. 8 Optimized reaction pathway for $CO_2$ hydrogenation to produce methanol, and potential energy diagram obtained by DFT calculation using $H_{26}Mo_{32}O_{96}$–$Pt_{20}$ slab model and schematic illustrations of the corresponding structure models in each reaction step.

Open Access Article. Published on 28 2021. Downloaded on 15-10-24 04.24.46.
This article is licensed under a Creative Commons Attribution-NonCommercial 3.0 Unported Licence.

interface is bridged by four Mo–O–Pt bonds was established (state **A** in Fig. 8). The calculated stepwise energy diagrams for $CO_2$ hydrogenation to methanol are depicted in Fig. 8 (the optimized structure models for each reaction step are presented in Fig. S11 in ESI†). Note that all the presented intermediate states were optimized after considering multiple possible pathways with the lowest energies. To begin with, three $H_2$ molecules are adsorbed into the slab model, which results in the formation of six dissociated H atoms on the $Pt_{20}$ cluster resulting in a large stabilization energy due to exothermic process (state **B**). The thus formed active H atoms are transferred to nearby surface terminal O atoms (states **C**, **D**), and then coordinated to the bi-bridging oxygen atom (states **E**, **F**), which eventually leads to the formation of $H_2O$ (state **G**) and an oxygen vacancy (state **H**) ($2H^+ + 2e^- + O_O \rightarrow H_2O + V_O$), coinciding well with the previous reports of O vacancy formation on $\alpha$-$MoO_3$.[58,59] The above reaction steps proceed with relatively low activation energies (**TS1** ~ **TS5**; $E_a$ < 28 kcal mol$^{-1}$) compared with the later reaction steps, while no possible pathways were found over a $H_{30}Mo_{32}O_{96}$ slab model without the $Pt_{20}$ cluster. Thus, an oxygen vacancy is likely to be formed *via* the H-spillover process involving the Pt NPs as illustrated in Scheme 1.

Next, one $CO_2$ molecule is adsorbed nearby the oxygen vacancy site (state **I**). As demonstrated for the oxygen-defective $H_{30}Mo_{32}O_{95}$ slab model (Fig. 4a), $CO_2$ is adsorbed and coordinated on the oxygen vacancy (state **J**) with an energy barrier of 46.0 kcal mol$^{-1}$ (**TS6**) to form the monodentate carbonate species (*O–C–O) or bidentate carbonate species ($CO_3^{2-}$) as intermediates, which is well consistent with the results obtained above whereby the oxygen vacancy is responsible for capturing and activating $CO_2$. The dissociation of the C=O bond of these intermediates occurs on the O vacancy site with an energy barrier of 20.1 kcal mol$^{-1}$ (**TS7**), and the dissociated *CO is stabilized by being adsorbed on the $Pt_{20}$ cluster (state **K**). The C=O bond cleavage on O vacancy site is corroborated by comparing the reaction paths on the different sites; over the perfect slab model without an oxygen vacancy, $CO_2$ molecule is stabilized most by being adsorbed on the $Pt_{20}$ cluster surface, and the path for *CO formation could not be explored. The dissociation of $CO_2$ on the $Pt_{20}$ cluster surface was found to involve a high energy barrier of 102.1 kcal mol$^{-1}$ (Fig. S12 in ESI†), which is 5-fold higher than that on the O vacancy site, indicating a low possibility of $CO_2$ dissociation on the Pt surface. Thus, the oxygen vacancy of $H_xMoO_{3-y}$ lowers the energy barriers for the cleavage of the C=O bond and functions as a deoxygenation center, rendering the Pt/$H_xMoO_{3-y}$ catalyst highly active towards $CO_2$ hydrogenation.

Subsequently, the *CO intermediate adsorbed on the $Pt_{20}$ cluster is hydrogenated by the active H atoms to finally produce methanol. The H atom on Pt first adds to the oxygen atom of the *CO (state **L**), which is followed by successive hydrogenation of the *COH intermediate to form *CHOH (state **M**), *$CH_2OH$ (state **N**), and finally to produce the desired *$CH_3OH$ (state **O**). The hydrogenation of *CO into *COH, *CHOH, *$CH_2OH$ and *$CH_3OH$ involves high energy barriers of 75.2, 13.2, 58.3, and 64.1 kcal mol$^{-1}$, respectively. In particular, the addition of the first H atom to *CO is required to overcome the highest energy barrier among all the TS's. This result suggests that CO serves as the main intermediate, and the rate-determining step of this reaction is the hydrogenation of the *CO intermediate (**TS8**), this being consistent with the reaction results and the kinetic analysis (Fig. 7).

We further explored the reaction paths for the production of CO and methane over the same slab model. Free CO can be formed from the *O–C–O intermediate with an energy barrier of 15.4 kcal mol$^{-1}$ (**TS7′**) (for optimized structure models, see Fig. S13 in ESI†), which is slightly lower than the energy barrier for the formation of the *CO intermediate adsorbed on the $Pt_{20}$ cluster (**TS7**: $E_a$ = 15.4 kcal mol$^{-1}$) and is significantly lower than those for methanol production from the *CO intermediate (**TS8**, **TS10**, **TS11**). This result indicates that gaseous CO formation is thermodynamically more favorable than the formation of methanol, being in line with the experimental results. Regarding methane production *via* hydrogenation of the *CO intermediate, possible intermediates and reaction pathways over the $H_{26}Mo_{32}O_{96}$–$Pt_{20}$ model were screened for. Given that the energy barrier for dehydration of *CHOH to form *CH ($E_a$ = 65.4 kcal mol$^{-1}$) was lower than those for dehydration of *COH ($E_a$ = 67.7 kcal mol$^{-1}$) and *$CH_2OH$ ($E_a$ = 118.3 kcal mol$^{-1}$), *CH is considered as the stable intermediate upon the formation of methane on the Pt/$H_xMoO_{3-y}$ catalyst (Fig. S14 in ESI†). The following hydrogenation of *CH proceeds *via* a stepwise formation of *$CH_2$, *$CH_3$ and $CH_4$ with reaction barriers of 20.1, 36.2 and 54.8 kcal mol$^{-1}$, respectively. The highest energy barrier to generate methanol from the *CHOH intermediate is 64.1 kcal mol$^{-1}$, which is lower than that for the transformation into methane ($E_a$ = 65.4 kcal mol$^{-1}$). Thus, methanol formation is energetically more favorable than methane formation over the Pt/$H_xMoO_{3-y}$ catalyst; hence the higher selectivity for methanol rather than for methane being well elucidated as demonstrated in the reaction experiments.

Based on comprehensive analyses of the reactions, *in situ* spectroscopic measurements and DFT calculations, we conclude that $CO_2$ hydrogenation to produce methanol over the Pt/$H_xMoO_{3-y}$ catalyst is achieved *via* oxygen vacancy-mediated "reverse Mars–van Kreveren" mechanism,[31,33,41,72] as illustrated

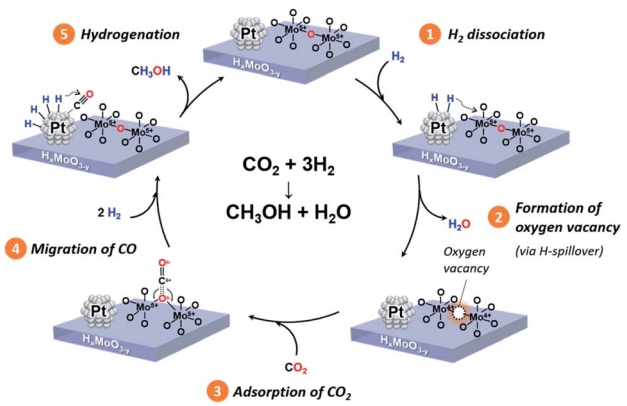


Scheme 2 Proposed reaction mechanism of $CO_2$ hydrogenation to produce methanol over the Pt/$H_xMoO_{3-y}$ catalyst.


© 2021 The Author(s). Published by the Royal Society of Chemistry

Open Access Article. Published on 28 2021. Downloaded on 15-10-24 04.24.46.
This article is licensed under a Creative Commons Attribution-NonCommercial 3.0 Unported Licence.

in Scheme 2. First, oxygen vacancies are formed in the $H_x$-$MoO_{3-y}$ sub-oxide during $H_2$ reduction through $H_2$ dissociation on the Pt NPs and the H-spillover process (steps 1 and 2). $CO_2$ is adsorbed on the oxygen vacancies and activated by the adjacent under-coordinated low-valence Mo centers ($Mo^{5+}/Mo^{4+}$) *via* electron donation with high adsorption energy, which induces the polarization of $CO_2$, weakening and then dissociation of the C=O bond. As a result, a CO intermediate is formed, and the oxygen vacancy is concurrently replenished with O atoms to restore an intact oxide surface (step 3). Based on the exploration by DFT calculation, the *CO intermediate is likely to migrate onto the Pt NP surface (step 4). The *CO intermediate reacts with active H species dissociated on the Pt NPs to initially form *COH species, which then undergo stepwise C–H bond formation, finally leading to the formation of methanol (step 5). A sole $H_xMoO_{3-y}$ works as a "reductant" but cannot be deemed as a "catalyst" for $CO_2$ reduction. On the contrary, the hybrid Pt/$H_xMoO_{3-y}$ catalyst developed in this study contains Pt NPs, which act as (i) active sites to supply dissociated H atoms to generate oxygen vacancies in Mo oxide and as (ii) active sites for hydrogenation of the CO intermediate to finally produce methanol (and methane). Owing to the high $H_2$ dissociation ability of the Pt NP (which occurs at around 140 °C, see Fig. 3a), the catalyst can sustain oxygen vacancies, and thus the catalytic cycle can be realized (steps 1 and 2). These catalytic cycles and the cooperative effect at the Pt–$H_xMoO_{3-y}$ interface facilitate efficient $CO_2$ hydrogenation under relatively mild reaction conditions.[38,74,75] The proposed reaction mechanism is totally different from the one known for the conventional Cu-based catalysts which normally require much higher reaction temperatures.[39,45,46]

In addition, recyclability of the Pt/$H_xMoO_{3-y}$(300) catalyst was investigated in recycling tests (Fig. S15 in ESI†). The Pt/$H_xMoO_{3-y}$(300) retained its catalytic activity for methanol production over multiple cycles; however, a continuous reduction of activity and methanol yield was observed. Characterization data including the XRD, XPS and XAFS results demonstrated that the structural variation of the $H_xMoO_{3-y}$ support was negligible even after the fourth cycle (see Fig. S16 in ESI†); however, TEM observation showed that the average Pt particle diameter of the spent catalyst apparently increased. As demonstrated above, the $CO_2$ deoxygenation is the dominant reaction at the interface between the Pt NPs and the $H_xMoO_{3-y}$ sub-oxide. Therefore, the reason for the continuous reduction in activity is probably due to the decreased number of Pt–$H_x$-$MoO_{3-y}$ interfacial sites due to the aggregation of the Pt NPs upon catalytic use,[78] hence making the cooperative effect less effective.

## Conclusions

In conclusion, the Pt/$H_xMoO_{3-y}$ hybrid catalyst was demonstrated to function as an efficient catalyst for $CO_2$ hydrogenation to produce methanol under relatively mild reaction conditions. The Pt NPs immobilized on a quasi-stable $H_x$-$MoO_{3-y}$ sub-oxide exhibited the highest $CO_2$ conversion and methanol yield among the oxide-supported Pt catalysts examined, with a methanol formation rate of 1.53 mmol $g_{\text{-cat}}^{-1}$ $h^{-1}$ in the liquid-phase $CO_2$ hydrogenation under relatively mild reaction conditions (total 4.0 MPa, 200 °C). Comprehensive analyses revealed that abundant surface oxygen vacancies and redox ability of Mo species in quasi-stable $H_xMoO_{3-y}$ endows this catalyst with enhanced adsorption and activation of $CO_2$ to produce a CO intermediate. As a result, the Pt NP can act as (i) a hydrogenation center to produce methanol from *CO species and as (ii) a site to supply active H atoms to regenerate oxygen vacancies *via* the H-spillover process. Thus, it has been clarified that $CO_2$ hydrogenation on the Pt/$H_xMoO_{3-y}$ catalyst is governed by the oxygen-vacancy-mediated "reverse Mars–van Krevelen" mechanism, which is promoted by the synergetic interaction between reducible Mo oxide as a $CO_2$-activation center and Pt NP as a $H_2$-activation center. For future development with the aim of large-scale implementation, further efforts to improve the reusability as well as to reduce the cost of the catalyst/process are needed. We expect that a continuous production of methanol/CO with a higher methanol selectivity is possible by employing a gas-phase fixed-bed reactor system, which can circumvent some problems in liquid-phase batch reactor system, such as catalyst deactivation, solvent use and post-separation process. The insights gained in this study is expected to provide a new avenue for manipulating catalytic properties *via* "oxygen vacancy engineering" approach and for advancing the mechanistic understanding of heterogeneous catalysis involving oxygen vacancies of metal oxides, which would contribute to the future development of more elaborated and high-performance catalysts for $CO_2$ hydrogenation.

## Author contributions

Y. Kuwahara led the conceptualization, design of the experiments, analysis and validation of the results, and wrote the manuscript. T. Mihogi, K. Hamahara and K. Kusu contributed to material synthesis, data collection, and formal analysis. H. Kobayashi contributed to the DFT calculation, formal analysis and data curation. H. Yamashita provided key advice and supervised the study.

## Conflicts of interest

There are no conflicts to declare.

## Acknowledgements

The present work was supported by JST, PRESTO (grant no. JPMJPR19T3), Japan, the Tonen General Sekiyu Research/Development Encouragement & Scholarship Foundation, and the Iwatani Naoji Foundation. A part of this work was supported by the grant for research of the Japan Petroleum Institute, 2018, awarded to Y. K. Y. K. and H. Y. thank Element Strategy Initiative of MEXT (grant no. JPMXP0112101003). The synchrotron radiation experiments for XAFS measurements were performed at the BL01B1 beam line in SPring-8 with the approval from JASRI (no. 2018B1185 and 2019A1050).

Open Access Article. Published on 28 2021. Downloaded on 15-10-24 04.24.46.
This article is licensed under a Creative Commons Attribution-NonCommercial 3.0 Unported Licence.

## Notes and references

1 J. Artz, T. E. Muller, K. Thenert, J. Kleinekorte, R. Meys, A. Sternberg, A. Bardow and W. Leitner, *Chem. Rev.*, 2018, **118**, 434–504.
2 A. J. Hunt, E. H. Sin, R. Marriott and J. H. Clark, *ChemSusChem*, 2010, **3**, 306–322.
3 E. V. Kondratenko, G. Mul, J. Baltrusaitis, G. O. Larrazábal and J. Pérez-Ramírez, *Energy Environ. Sci.*, 2013, **6**, 3112–3135.
4 E. A. Quadrelli, G. Centi, J. L. Duplan and S. Perathoner, *ChemSusChem*, 2011, **4**, 1194–1215.
5 A. Alvarez, A. Bansode, A. Urakawa, A. V. Bavykina, T. A. Wezendonk, M. Makkee, J. Gascon and F. Kapteijn, *Chem. Rev.*, 2017, **117**, 9804–9838.
6 M. D. Porosoff, B. Yan and J. G. Chen, *Energy Environ. Sci.*, 2016, **9**, 62–73.
7 R. Sun, Y. Liao, S.-T. Bai, M. Zheng, C. Zhou, T. Zhang and B. F. Sels, *Energy Environ. Sci.*, 2021, **14**, 1247–1285.
8 A. Karelovic, G. Galdames, J. C. Medina, C. Yévenes, Y. Barra and R. Jiménez, *J. Catal.*, 2019, **369**, 415–426.
9 R. P. Ye, J. Ding, W. Gong, M. D. Argyle, Q. Zhong, Y. Wang, C. K. Russell, Z. Xu, A. G. Russell, Q. Li, M. Fan and Y. G. Yao, *Nat. Commun.*, 2019, **10**, 5698.
10 Z. Ma and M. D. Porosoff, *ACS Catal.*, 2019, **9**, 2639–2656.
11 D. R. Palo, *Chem. Rev.*, 2007, **107**, 3992–4021.
12 K. C. Waugh, *Catal. Lett.*, 2012, **142**, 1153–1166.
13 M. Saito, *Catal. Surv. Jpn.*, 1998, **2**, 175–184.
14 G. A. Olah, *Angew. Chem., Int. Ed.*, 2013, **52**, 104–107.
15 G. A. Olah, A. Goeppert and G. K. S. Prakash, *J. Org. Chem.*, 2009, **74**, 487–498.
16 R. Gaikwad, A. Bansode and A. Urakawa, *J. Catal.*, 2016, **343**, 127–132.
17 W. H. Wang, Y. Himeda, J. T. Muckerman, G. F. Manbeck and E. Fujita, *Chem. Rev.*, 2015, **115**, 12936–12973.
18 Y. Chen, S. Choi and L. T. Thompson, *ACS Catal.*, 2015, **5**, 1717–1725.
19 S. Kar, A. Goeppert, J. Kothandaraman and G. K. S. Prakash, *ACS Catal.*, 2017, **7**, 6347–6351.
20 J. Kothandaraman, A. Goeppert, M. Czaun, G. A. Olah and G. K. Prakash, *J. Am. Chem. Soc.*, 2016, **138**, 778–781.
21 N. M. Rezayee, C. A. Huff and M. S. Sanford, *J. Am. Chem. Soc.*, 2015, **137**, 1028–1031.
22 S. Wesselbaum, V. Moha, M. Meuresch, S. Brosinski, K. M. Thenert, J. Kothe, T. V. Stein, U. Englert, M. Holscher, J. Klankermayer and W. Leitner, *Chem. Sci.*, 2015, **6**, 693–704.
23 S. Bai, Q. Shao, Y. Feng, L. Bu and X. Huang, *Small*, 2017, **13**, 1604311.
24 M. U. Khan, L. Wang, Z. Liu, Z. Gao, S. Wang, H. Li, W. Zhang, M. Wang, Z. Wang, C. Ma and J. Zeng, *Angew. Chem., Int. Ed.*, 2016, **55**, 9548–9552.
25 H. Li, L. Wang, Y. Dai, Z. Pu, Z. Lao, Y. Chen, M. Wang, X. Zheng, J. Zhu, W. Zhang, R. Si, C. Ma and J. Zeng, *Nat. Nanotechnol.*, 2018, **13**, 411–417.
26 T. Toyao, S. Kayamori, Z. Maeno, S. M. A. H. Siddiki and K.-i. Shimizu, *ACS Catal.*, 2019, **9**, 8187–8196.
27 Z. He, Q. Qian, J. Ma, Q. Meng, H. Zhou, J. Song, Z. Liu and B. Han, *Angew. Chem., Int. Ed.*, 2016, **55**, 737–741.
28 X. Zheng, Y. Lin, H. Pan, L. Wu, W. Zhang, L. Cao, J. Zhang, L. Zheng and T. Yao, *Nano Res.*, 2018, **11**, 2357–2365.
29 W. Zhang, L. Wang, H. Liu, Y. Hao, H. Li, M. U. Khan and J. Zeng, *Nano Lett.*, 2017, **17**, 788–793.
30 K. W. Ting, T. Toyao, S. M. A. H. Siddiki and K.-i. Shimizu, *ACS Catal.*, 2019, **9**, 3685–3693.
31 D. Ferri, T. Bürgi and A. Baiker, *Phys. Chem. Chem. Phys.*, 2002, **4**, 2667–2672.
32 G. Zhuang, Y. Chen, Z. Zhuang, Y. Yu and J. Yu, *Sci. China Mater.*, 2020, **63**, 2089–2118.
33 L. F. Bobadilla, J. L. Santos, S. Ivanova, J. A. Odriozola and A. Urakawa, *ACS Catal.*, 2018, **8**, 7455–7467.
34 B. J. Hare, D. Maiti, Y. A. Daza, V. R. Bhethanabotla and J. N. Kuhn, *ACS Catal.*, 2018, **8**, 3021–3029.
35 J. Ye, C. Liu, D. Mei and Q. Ge, *ACS Catal.*, 2013, **3**, 1296–1306.
36 G. Xi, S. Ouyang, P. Li, J. Ye, Q. Ma, N. Su, H. Bai and C. Wang, *Angew. Chem., Int. Ed.*, 2012, **51**, 2395–2399.
37 J. Li, Y. Ye, L. Ye, F. Su, Z. Ma, J. Huang, H. Xie, D. E. Doronkin, A. Zimina, J.-D. Grunwaldt and Y. Zhou, *J. Mater. Chem. A*, 2019, **7**, 2821–2830.
38 J. A. Rodriguez, P. Liu, D. J. Stacchiola, S. D. Senanayake, M. G. White and J. G. Chen, *ACS Catal.*, 2015, **5**, 6696–6706.
39 K. Larmier, W. C. Liao, S. Tada, E. Lam, R. Verel, A. Bansode, A. Urakawa, A. Comas-Vives and C. Coperet, *Angew. Chem., Int. Ed.*, 2017, **56**, 2318–2323.
40 M. S. Frei, C. Mondelli, R. Garcia-Muelas, K. S. Kley, B. Puertolas, N. Lopez, O. V. Safonova, J. A. Stewart, D. Curulla Ferre and J. Perez-Ramirez, *Nat. Commun.*, 2019, **10**, 3377.
41 Y. Kuwahara, Y. Yoshimura, K. Haematsu and H. Yamashita, *J. Am. Chem. Soc.*, 2018, **140**, 9203–9210.
42 L. Chen, A. C. Cooper, G. P. Pez and H. Cheng, *J. Phys. Chem. C*, 2008, **112**, 1755–1758.
43 H. Cheng, L. Chen, A. C. Cooper, X. Sha and G. P. Pez, *Energy Environ. Sci.*, 2008, **1**, 338–354.
44 H. Cheng, T. Kamegawa, K. Mori and H. Yamashita, *Angew. Chem., Int. Ed.*, 2014, **53**, 2910–2914.
45 P. Liu, Y. Yang and M. G. White, *Surf. Sci. Rep.*, 2013, **68**, 233–272.
46 S. Kattel, P. Liu and J. G. Chen, *J. Am. Chem. Soc.*, 2017, **139**, 9739–9754.
47 J. J. Birtill and P. G. Dickens, *Mater. Res. Bull.*, 1978, **13**, 311–316.
48 S. Adams, *J. Solid State Chem.*, 2000, **149**, 75–87.
49 B. Braïda, S. Adams and E. Canadell, *Chem. Mater.*, 2005, **17**, 5957–5969.
50 N. A. Chernova, M. Roppolo, A. C. Dillon and M. S. Whittingham, *J. Mater. Chem.*, 2009, **19**, 2526–2552.
51 X. W. Lou and H. C. Zeng, *Chem. Mater.*, 2002, **14**, 4781–4789.
52 P. A. Sermon and G. C. Bond, *Catal. Rev.*, 1973, **8**, 211–239.
53 S. Masuda, K. Shun, K. Mori, Y. Kuwahara and H. Yamashita, *Chem. Sci.*, 2020, **11**, 4194–4203.
54 P. A. Sermon and G. C. Bond, *J. Chem. Soc., Faraday Trans. 1*, 1976, **72**, 730–744.


© 2021 The Author(s). Published by the Royal Society of Chemistry

Open Access Article. Published on 28 2021. Downloaded on 15-10-24 04.24.46.
This article is licensed under a Creative Commons Attribution-NonCommercial 3.0 Unported Licence.

55 R. Erre, H. van Damme and J. J. Fripiat, *Surf. Sci.*, 1983, **127**, 48–68.
56 R. Erre, H. van Damme and J. J. Fripiat, *Surf. Sci.*, 1983, **127**, 69–82.
57 J. G. Kim and J. R. Regalbuto, *J. Catal.*, 1993, **139**, 175–190.
58 Y.-H. Lei and Z.-X. Chen, *J. Phys. Chem. C*, 2012, **116**, 25757–25764.
59 J. Z. Ou, J. L. Campbell, D. Yao, W. Wlodarski and K. Kalantar-zadeh, *J. Phys. Chem. C*, 2011, **115**, 10757–10763.
60 M. Vasilopoulou, A. M. Douvas, D. G. Georgiadou, L. C. Palilis, S. Kennou, L. Sygellou, A. Soultati, I. Kostis, G. Papadimitropoulos, D. Davazoglou and P. Argitis, *J. Am. Chem. Soc.*, 2012, **134**, 16178–16187.
61 H. Cheng, M. Wen, X. Ma, Y. Kuwahara, K. Mori, Y. Dai, B. Huang and H. Yamashita, *J. Am. Chem. Soc.*, 2016, **138**, 9316–9324.
62 H. Cheng, X. Qian, Y. Kuwahara, K. Mori and H. Yamashita, *Adv. Mater.*, 2015, **27**, 4616–4621.
63 H. S. Kim, J. B. Cook, H. Lin, J. S. Ko, S. H. Tolbert, V. Ozolins and B. Dunn, *Nat. Mater.*, 2017, **16**, 454–460.
64 A. Borgschulte, O. Sambalova, R. Delmelle, S. Jenatsch, R. Hany and F. Nuesch, *Sci. Rep.*, 2017, **7**, 40761.
65 J. J. Birtill and P. G. Dickens, *J. Solid State Chem.*, 1979, **29**, 367–372.
66 N. Sotani, K. Eda, M. Sadamitu and S. Takagi, *Bull. Chem. Soc. Jpn.*, 1989, **62**, 903–907.
67 S. Chen, H. Wang, Z. Kang, S. Jin, X. Zhang, X. Zheng, Z. Qi, J. Zhu, B. Pan and Y. Xie, *Nat. Commun.*, 2019, **10**, 788.
68 X. Yang, S. Wang, N. Yang, W. Zhou, P. Wang, K. Jiang, S. Li, H. Song, X. Ding, H. Chen and J. Ye, *Appl. Catal., B*, 2019, **259**, 118088.
69 R. Radhakrishnan, C. Reed, S. T. Oyama, M. Seman, J. N. Kondo, K. Domen, Y. Ohminami and K. Asakura, *J. Phys. Chem. B*, 2001, **105**, 8519–8530.
70 Y. N. Zhou, J. Ma, E. Hu, X. Yu, L. Gu, K. W. Nam, L. Chen, Z. Wang and X. Q. Yang, *Nat. Commun.*, 2014, **5**, 5381.
71 P. Mars and D. W. van Krevelen, *Chem. Eng. Sci.*, 1954, **3**, 41–59.
72 A. V. Mironenko and D. G. Vlachos, *J. Am. Chem. Soc.*, 2016, **138**, 8104–8113.
73 S. Gaur, H. Wu, G. G. Stanley, K. More, C. S. S. R. Kumar and J. J. Spivey, *Catal. Today*, 2013, **208**, 72–81.
74 Y. F. Li, W. Lu, K. Chen, P. Duchesne, A. Jelle, M. Xia, T. E. Wood, U. Ulmer and G. A. Ozin, *J. Am. Chem. Soc.*, 2019, **141**, 14991–14996.
75 Y. F. Li, N. Soheilnia, M. Greiner, U. Ulmer, T. Wood, A. A. Jelle, Y. Dong, A. P. Yin Wong, J. Jia and G. A. Ozin, *ACS Appl. Mater. Interfaces*, 2019, **11**, 5610–5615.
76 S. Bai, Q. Shao, P. Wang, Q. Dai, X. Wang and X. Huang, *J. Am. Chem. Soc.*, 2017, **139**, 6827–6830.
77 A. Lubezky, L. Chechelnitsky and M. Folman, *J. Chem. Soc., Faraday Trans.*, 1996, **92**, 2269–2274.
78 H. Bahruji, M. Bowker, G. Hutchings, N. Dimitratos, P. Wells, E. Gibson, W. Jones, C. Brookes, D. Morgan and G. Lalev, *J. Catal.*, 2016, **343**, 133–146.

© 2021 The Author(s). Published by the Royal Society of Chemistry